

# Local aggregate multiscale processes: A scalable, machine-learning-compatible spatial model

Daisuke Murakami<sup>1,\*</sup>, Alexis Comber<sup>2</sup>, Takahiro Yoshida<sup>3</sup>,  
Narumasa Tsutsumida<sup>4</sup>, Chris Brunsdon<sup>5</sup>, Tomoki Nakaya<sup>6</sup>

<sup>1</sup> Department of Fundamental Statistical Mathematics, Japan (E-mail: [dmuraka@ism.ac.jp](mailto:dmuraka@ism.ac.jp))

<sup>2</sup> School of Geography, University of Leeds, UK

<sup>3</sup> Center for Spatial Information Science, the University of Tokyo, Japan

<sup>4</sup> Graduate School of Science & Engineering, Saitama University, Saitama, Japan

<sup>5</sup> National Center for Geocomputation, National University of Ireland Maynooth, Ireland

<sup>6</sup> Graduate School of Environment Studies, Tohoku University, Japan

Abstract: This study develops the Local Aggregate Multiscale Process (LAMP), a scalable and machine-learning-compatible alternative to conventional spatial Gaussian processes (GPs, or kriging).

Unlike conventional covariance-based spatial models, LAMP represents spatial processes by a multiscale ensemble of local models, inspired by geographically weighted regression. To ensure stable model training, larger-scale patterns that are easier to learn are modeled first, followed by smaller-scale patterns, with training terminated once the validation score stops improving. The training procedure, which is based on holdout validation, is easily integrated with other machine learning algorithms (e.g., random forests and neural networks). LAMP training is computationally efficient as it avoids explicit matrix inversion, a major computational bottleneck in conventional GPs. Comparative Monte Carlo experiments demonstrate that LAMP, as well as its integration with random

forests, achieves superior predictive performance compared to existing models. Finally, we apply the proposed methods to an analysis of residential land prices in the Tokyo metropolitan area, Japan.

## 1. Introduction

Modeling spatial processes is the central topic in spatial statistics. Gaussian processes (GPs; Williams and Rammussen, 1995; Cressie, 2015) are widely used to represent spatially dependent processes using a distance-decaying covariance/correlation function. As explained in Gelfand et al. (2010), GPs have been used for various purposes, including spatial and spatiotemporal predictions, regression analysis, and uncertainty quantification.

GPs have difficulties in terms of (i) scalability for large samples and (ii) flexibility. Regarding (i), GPs are applicable only to small-to-moderate samples due to the need to invert an  $N \times N$  covariance matrix, with computational complexity rapidly increasing at the order of  $N^3$ , where  $N$  is the sample size. To mitigate the problem, fast GP approximations have been proposed (see Heaton, 2019; Liu et al., 2020; Hazra et al., 2025 for review). Representative approaches include basis function approximation (see Cressie et al., 2022 for review), which represents map patterns using  $L$  ( $\ll N$ ) spatial basis functions, and sparse covariance/precision matrix approximation, which assumes (conditional) independence from distant samples.

Basis function approximations include fixed rank kriging (Cressie and Johannesson, 2008), additive models (Wood, 2017), and stochastic partial differential equation (SPDE) models (Bakka et al., 2018). Although they are particularly computationally efficient, they tend to overlook small-scale spatial variations, leading to reduced modeling accuracy (Murakami et al., 2024). Sparse approximations include the nearest-neighbor GP (NNGP; Datta et al., 2016) and other Vecchia approximations (Katzfuss and Guinness, 2021). They tend to capture small-scale patterns accurately, but often introduce noise when the true process exhibits large-scale patterns, as we will demonstrate later. It remains an important research issue to develop fast spatial process models that accurately describe both large- and small-scale map patterns.

Regarding (ii) flexibility, spatial GPs are suitable for modeling continuous map patterns, but less suitable for modeling other patterns including discontinuous and/or non-linear patterns. For instance, in land price modeling, spatial GPs are less suitable for capturing abrupt changes in price levels between areas separated by physical or institutional barriers such as rivers, roads, or zoning regulations. As suggested in Yoshida et al. (2023), the resulting spatial prediction accuracy of GPs are often lower than other machine learning algorithms such as random forest (Breiman, 2001) and gradient boosting (Freidman, 2002), particularly when many covariates/features are available. Although Gaussian spatial models have been integrated with random forests (e.g., Georanos et al., 2021), gradient boosting (Sigrist, 2022), and neural networks (e.g., Chen et al., 2020; Zammit-

Mangion et al., 2022; Zhan and Datta, 2025), further studies are necessary to better leverage GP's efficiency in modeling smooth patterns by integrating them within machine learning algorithms to model non-smooth complex patterns.

A major bottleneck to achieving such integration lies in the differences between model optimization frameworks. Spatial regression models are typically estimated through likelihood-based approaches, supplemented with priors in the case of Bayesian inference. In contrast, machine learning algorithms are typically optimized using validation methods. To facilitate integration, it would be useful to develop a spatial process model that can be optimized via validation.

To address these background issues related to scalability and flexibility, this paper develops a fast validation-based spatial modeling framework. For better scalability, we develop a novel spatial process called Local Aggregate Multiscale Process (LAMP), inspired by geographically weighted regression (GWR; Brunson et al., 1996; Fotheringham et al., 2017; Lu et al., 2018; Comber et al., 2023). A fast sequential algorithm is developed to stably model LAMP and to support its integration with other machine learning algorithms.

The remainder of the sections are organized as follows. Section 2 introduces a local model, and Section 3 extends it to the LAMP. Section 4 compares the LAMP with alternatives spatial models through Monte Carlo experiments, and Section 5 applies the proposed method to a land price analysis.

Finally, Section 6 illustrates the method using an empirical case study and extensively discusses the results before some conclusions are drawn in Section 7.

## 2. Local model

Suppose that data  $y(s_i)$  are observed at the  $i$ -th sample site  $s_i$  in a study region  $D \subset \mathbb{R}^2$ , where  $i \in \{1, \dots, N\}$ . A local model centered at site  $s_c$  expresses the data distribution as follows:

$$y(s_i)|c \sim N\left(\mu_c, \frac{\sigma_c^2}{w_h^2(d_{i,c})}\right), \quad \mu_c \sim N(0, \tau_c^2), \quad (1)$$

depending on the local mean  $\mu_c$  and variance  $\sigma_c^2$  near the center. A Gaussian prior with variance  $\tau_c^2$  is imposed on  $\mu_c$  to regularize the estimate. The spatial weight  $w_h(d_{i,c})$  is defined by a kernel function that decays with distance  $d_{i,c}$  from the center  $s_c$ . While various distance and kernel functions are available, we consider the Gaussian kernel  $w_h(d_{i,c}) = \exp\left(-\frac{d_{i,c}^2}{h^2}\right)$  and the exponential kernel  $w_h(d_{i,c}) = \exp\left(-\frac{d_{i,c}}{h}\right)$  with Euclidean distance, both of which are commonly used in spatial statistics (e.g., Fotheringham et al., 2009; Cressie, 2015). A kernel with a small bandwidth  $h$  assigns weights only to nearby samples to accurately capture local patterns, whereas a large bandwidth assigns weights to both nearby and distant samples to accurately capture larger-scale patterns.

Eq. (1) is an intercept-only penalized regression. The least squares estimator of  $\mu_c$  equals:

$$\hat{\mu}_c = \frac{\sum_{i=1}^N w_h^2(d_{i,c}) y(s_i)}{\sum_{i=1}^N w_h^2(d_{i,c}) + \frac{\hat{\sigma}_c^2}{\tau_c^2}}, \quad (2)$$

where the unbiased estimate of  $\sigma_c^2$  equals  $\hat{\sigma}_c^2 = \frac{\sum_{i=1}^N w_h^2(d_{i,c})(y(s_i) - \mu_c)^2}{N-1}$ , and the variance  $\tau_c^2$  of  $\mu_c$

may be determined by prior knowledge as we will do later.

The predictive distribution of  $y(s_i)$  given the local model is represented as  $y(s_i)|c \sim N(\hat{\mu}_c, \hat{\sigma}_c^2(s_i))$  in which the predictive variance  $\hat{\sigma}_c^2(s_i)$  is obtained following the standard linear algebra for the simple penalized regression, as follows:

$$\hat{\sigma}_c^2(s_i) = \frac{\hat{\sigma}_c^2}{\sum_{i=1}^N w_h^2(d_{i,c}) + \frac{\hat{\sigma}_c^2}{\tau_c^2}} + \frac{\hat{\sigma}_c^2}{w_h^2(d_{i,c})}, \quad (3)$$

As illustrated in Figure 1, the prediction interval, determined by the variance  $\hat{\sigma}_c^2(s_i)$ , is narrow near the center  $s_c$  while extremely wide in other regions, indicating that the local model has explanatory power only in the vicinity of the center. Therefore, we will aggregate multiple local models to construct spatial processes covering entire region as detailed later.

In distributional form, the local model can be expressed as follows:<sup>1</sup>

$$p(y(s_i)|c) \propto p(y(s_i)|\mu_c, \sigma_c^2) w_h^2(d_{i,c}) p(\mu_c|0, \tau_c^2). \quad (4)$$

where  $p(y(s_i)|\mu_c, \sigma_c^2)$  is the probability density function of  $y(s_i) \sim N(\mu_c, \sigma_c^2)$  and  $p(\mu_c|0, \tau_c^2)$  is similarly defined. The next section introduces a spatial process that is constructed by aggregating multiple local models using Eq. (4).

---

<sup>1</sup> The probability density function of  $y(s_i)|c \sim N(\mu_c, \sigma^2/w_h^2(d_{i,c}))$  equals  $p(y(s_i)|c) = \frac{w_h^2(d_{i,c})}{\sqrt{2\pi}\sigma} \exp\left(-\frac{w_h^2(d_{i,c})}{2\sigma^2}(y(s_i) - \mu_c)^2\right) = w_h^2(d_{i,c}) \frac{1}{\sqrt{2\pi}\sigma} \exp\left(-\frac{1}{2\sigma^2}(y(s_i) - \mu_c)^2\right) w_h^2(d_{i,c}) = w_h^2(d_{i,c}) p(y(s_i)|\mu_c, \sigma_h^2) w_h^2(d_{i,c}) \propto p(y(s_i)|\mu_c, \sigma_h^2) w_h^2(d_{i,c})$ .

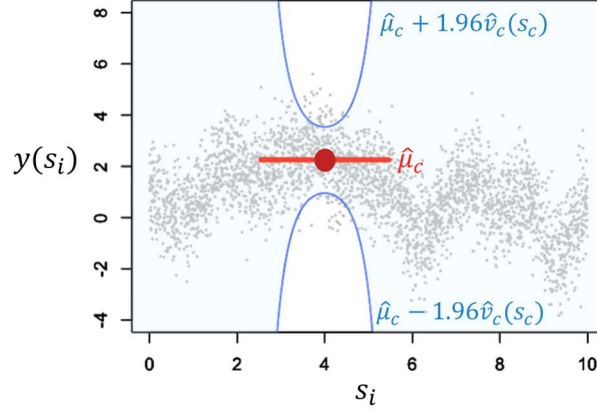


Figure 1: Mean estimate  $\hat{\mu}_c$  (red) and the 95% confidence interval (blue;  $\hat{\mu}_c \pm 1.96\hat{\sigma}_c^2(s_i)$ ) of the local model centered on  $s_c = 4.0$  (red/brown dot) in one-dimensional space. Synthetic samples (grey dots;  $N= 3,000$ ) are generated from a moving average process, and a local model with a Gaussian kernel ( $h = 0.8$ ) is fitted.

### 3. Local aggregate multiscale process (LAMP)

This section develops the LAMP. Section 3.1 introduces the multiscale model structure, and Section 3.2 describes the single-scale processes that comprise the model.

#### 3.1. Model structure

The LAMP is a multiscale spatial process defined as follows:

$$z_{1:R}(s_i) = \sum_{r=1}^R z_r(s_i), \quad z_r(s_i) \sim N(\hat{z}_r(s_i), \sigma_r^2(s_i)). \quad (5)$$

$z_r(s_i)$  is the single-scale processes in resolution  $r$ . The spatial scale is determined by the kernel bandwidth  $h_r$ , where  $h_{r+1} = \delta h_r$  and  $0 < \delta < 1$ . In other words,  $z_1(s_i)$  represents the largest-scale process,  $z_2(s_i)$  represents the second largest scale process, and  $z_R(s_i)$  is the  $R$ -th largest-scale or the smallest-scale process. The terminal resolution  $R$  is assumed to be unknown; it will be large if data have small-scale spatial patterns.

## 3.2. Single-scale process

### 3.2.1. Local models

We construct the process  $z_r(s_i)$  at resolution  $r$  by aggregating (averaging)  $C_r$  local models, which are defined following Section 2, as follows:

$$z_r(s_i)|c_r \sim N\left(\mu_{c_r}, \frac{\sigma_{c_r}^2}{w_{h_r}^2(d_{i,c_r})}\right), \quad \mu_{c_r} \sim N(0, \tau_{c_r}^2), \quad (6)$$

which has the following distribution form (see Eq. 4):

$$p(z_r(s_i)|c_r) \propto p(z_r(s_i)|\mu_{c_r}, \sigma_{c_r}^2)^{w_{h_r}^2(d_{i,c_r})} p(\mu_{c_r}|0, \tau_{c_r}^2). \quad (7)$$

The local model explains only the local pattern near its kernel center as demonstrated in Figure 1. To capture patterns across the entire study area, we place multiple kernel centers so that their windows collectively cover the region. Following Kumar et al. (2012), who showed that  $k$ -means cluster centers effectively represent sample sites, we define the kernel centers as the sample sites closest to the  $k$ -means cluster centers.

The number of centers  $C_r$  is sufficient as long as the kernel windows (areas within the distance  $h$  from each center) cover the entire region. For example, consider data distributed over the interval  $[0,10]$  with length  $D = 10$ . If the bandwidth equals  $h_r = 1$ , then, placing  $D/h_r = 10$  kernel centers at regular intervals ensures that every point in  $[0, 10]$  falls within more than one kernel window. Even with the  $k$ -means-based centers,  $C_r = \text{round}(1.5D/h_r)$  kernels would be sufficient to achieve comparable coverage as illustrated in Figure 2, where  $\text{round}(\cdot)$  denotes rounding to the nearest integer.

Similarly, in two-dimensional case, we set the number of centers as  $C_r = \text{round}(1.5D^2/h_r^2)$  where  $D$  is the diagonal length of the bounding square containing all sample sites.  $D^2$  represents the area of the bounding square, while  $h_r^2$  approximates the coverage area of each kernel. This criterion ensures that the total sum of the coverage area of the  $C_r$  kernels is about 1.5 times the area of the square  $D^2$  (i.e.,  $h_r^2 C_r \approx 1.5D^2$ ), providing a practical guideline that yields sufficiently large number of centers to cover the entire region as demonstrated in Figure 3.

Note that alternative criteria for determining the number and placement of kernels are possible and merit further investigation in future work.

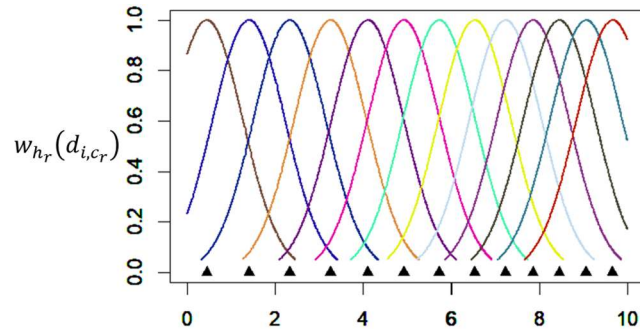


Figure 2: Kernels placed in the interval  $[0,10]$  ( $D = 10$ ). For a bandwidth of  $h_r = 1.16$ , the number of centers is given by  $C_r = \text{round}(1.5D/h_r) = 13$ . These centers (black triangles) are selected from 3,000 sample sites shown in Figure 1.

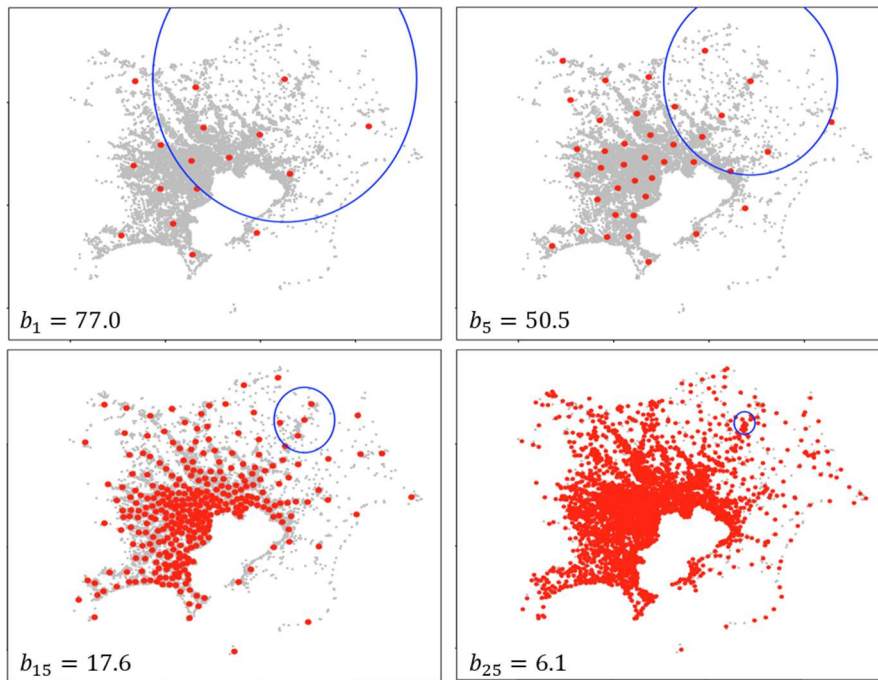


Figure 3: An example of kernel centers (red) in two-dimensions for  $r \in \{1,5,15,25\}$ . The centers are selected from land price assessment sites (grey; see Section 5). For each  $r$ , blue circles indicate window of a kernel with radius  $b_r$ . They are later used to construct spatial processes in Section 5.

### 3.2.2. Aggregation of local models

Each local model is estimated using local samples with  $w_{h_r}(d_{i,c_r}) > 0.05$ , and these sub-samples may overlap. Since each local model explains patterns only around its kernel center as shown in Figure 1, such overlap is necessary; without it, areas distant from local centers could not be explained even if they are aggregated.

To aggregate local models, sophisticated methods such as product-of-experts (PoE) and Bayesian committee machine (see, Cohen et al., 2020) have been developed. However, they generally require non-overlapping sub-samples for each model while we assumed overlapped sub-samples. Exceptionally, generalized PoE (gPoE; Cao and Fleet, 2014) allows overlapped sub-samples, which align with our setting. Accordingly, we use gPoE to aggregate  $C_r$  local models.

gPoE takes a weighted product of model's probability density functions to aggregate them.

In our case, the aggregated model yields (see Eq. 7):

$$p(z_r(s_i)|1_r, \dots, C_r) \propto \prod_{c_r=1}^{C_r} p(z_r(s_i)|\mu_{c_r}, \sigma_{c_r}^2)^{w_r(d_{i,c_r})} p(\mu_{c_r}|0, \tau_{c_r}^2), \quad (8)$$

which is an ensemble of local models weighted by the spatial kernel  $w_r(d_{i,c_r})$ .

Interestingly, as detailed in Cao and Fleet (2014), the gPoE aggregated process (Eq. 8) is expressed simply by  $z_r(s_i) \sim N(\hat{z}_r(s_i), \sigma_r^2(s_i))$  where

$$\hat{z}_r(s_i) = \sigma_r^2(s_i) \sum_{c_r=1}^{C_r} \frac{w_r(d_{i,c_r})}{\sigma_{c_r}^2} \mu_{c_r}, \quad (9)$$

$$\sigma_r^2(s_i) = 1 / \sum_{c_r=1}^{C_r} \frac{w_r(d_{i,c_r})}{\sigma_{c_r}^2}. \quad (10)$$

The predictive mean (Eq. 9) is defined by a weighted average of the local means  $\mu_{c_r}$ , with weights  $\frac{w_r(d_{i,c_r})}{\sigma_{c_r}^2}$ , which emphasize local models that are both nearby and accurate.

As shown in Figure 4, the aggregated processes flexibly capture latent patterns at a scale determined by the bandwidth. Nevertheless, the resulting process underfits when  $h_r$  is too large and overfits when it is too small. The next section develops an algorithm that optimally synthesizes these scale-wise processes while avoiding both underfitting and overfitting.

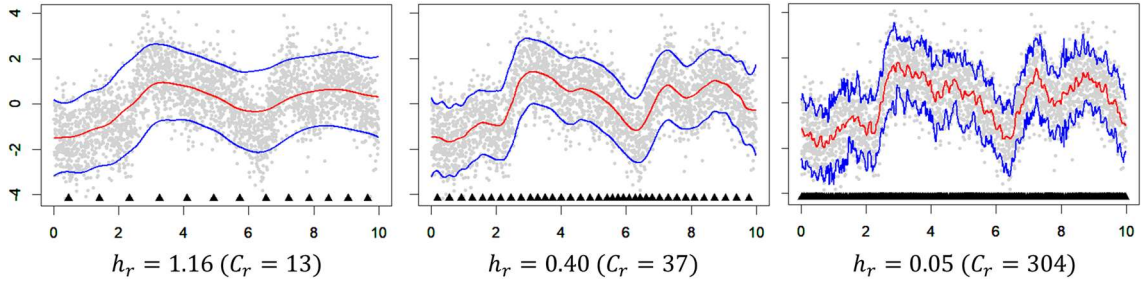


Figure 4: Predictive mean (red;  $\hat{z}_r(s_i)$ ) and 95% confidence interval (blue;  $\hat{z}_r(s_i) \pm 1.96\sigma(s_i)$ ) of the aggregated processes  $z_r(s_i) \sim N(\hat{z}_r(s_i), \sigma_r^2(s_i))$  for  $h_r \in \{1.16, 0.40, 0.05\}$ . The processes are obtained by individually fitting  $C_r$  local models for the 3,000 samples generated from a moving average process, and aggregating them using Eqs. (9) and (10). Black triangles at the bottom of each panel indicate the  $C_r$  kernel centers. See Figure 2 for the 13 kernels used to construct the aggregated process with  $h_r = 1.16$ .

## 4. Learning algorithms

After introducing our full model and learning algorithm in Section 4.1, Section 4.2 presents details of the algorithm for a linear LAMP model. Section 4.3 describes another algorithm for a non-linear LAMP model in which the non-linearity is expressed by a machine learning model.

### 4.1. Outline

This study assumes the following structure for data:

$$\begin{aligned} y(s_i) &= \mathbf{x}(s_i)' \boldsymbol{\beta} + f(\mathbf{x}_f(s_i)) + z_{1:R}(s_i) + e(s_i), & e(s_i) &\sim N(0, \sigma^2(s_i)), \\ z_{1:R}(s_i) &= \sum_{r=1}^R z_r(s_i), & z_r(s_i) &\sim N(\hat{z}_r(s_i), \sigma_r^2(s_i)), \end{aligned} \tag{11}$$

where  $\mathbf{x}(s_i)$  is a vector of covariates and  $\boldsymbol{\beta}$  is a vector of their coefficients. The model consists of a linear term  $\mathbf{x}(s_i)' \boldsymbol{\beta}$ , a non-linear term  $f(\mathbf{x}_f(s_i))$  that captures non-linearity and/or higher-order interactions in the covariate vector  $\mathbf{x}_f(s_i)$ . the spatial process  $z_{1:R}(s_i)$  defined by LAMP (Eq. 5), and noise  $e(s_i)$  with variance  $\sigma^2(s_i)$ . The function  $f(\mathbf{x}_f(s_i))$  may be specified using random forests, gradient boosting trees, or neural networks.

Unfortunately, our preliminary analysis indicated that the simultaneous optimization of  $z_1(s_i), \dots, z_R(s_i), f(\mathbf{x}_f(s_i))$  is unstable and computationally inefficient. To address this, we adopt a sequential estimation procedure that first estimates simpler, easier to learn patterns, followed by more complex patterns (see Soviany et al., 2022). This approach avoids heavy simultaneous optimization,

and prioritizing simpler terms naturally yields a simpler output model, resulting in more stable optimization. In our case, an appropriate learning order is  $z_1(s_i), \dots, z_R(s_i), f(\mathbf{x}_f(s_i))$  for the following reasons:  $z_r(s_i)$  involves an increasing number of hyperparameters ( $\mu_{C_r}, \sigma_{C_r}^2, \tau_{C_r}^2$  for each of the  $C_r$  local models) as  $r$  grows;  $f(\mathbf{x}_f(s_i))$  is assumed as a complex non-linear function.

Sections 4.2 and 4.3 develop our estimation procedure for the linear LAMP model with  $f(\mathbf{x}_f(s_i)) = 0$ , and for the non-linear LAMP model, which optimizes  $f(\mathbf{x}_f(s_i))$ , respectively.

## 4.2. Linear LAMP model

This section explains the estimation procedure of the following model with  $f(\mathbf{x}_f(s_i)) = 0$ :

$$y(s_i) = \mathbf{x}(s_i)' \boldsymbol{\beta} + z_{1:R}(s_i) + e(s_i), \quad e(s_i) \sim N(0, \sigma^2(s_i)), \quad (12)$$

Unlike conventional spatial regression models which are typically estimated via likelihood-based inference, we adopt holdout validation (HV) which randomly divides the data into  $100\varphi$  % training samples and  $100(1 - \varphi)$  % validation samples, with  $\varphi$  set to 0.75. In other words, 75 % of the samples are used to estimate the model, while the remaining samples are used to evaluate its predictive error, measured by the sum-of squared error (SSE). The SSE for the validation samples indexed by  $i_v \in \{1, \dots, N_v\}$  is given as  $SSE_R = \sum_{i_v=1}^{N_v} \left( y(s_{i_v}) - \mathbf{x}(s_{i_v})' \hat{\boldsymbol{\beta}} - \hat{z}_{1:R}(s_{i_v}) \right)^2$ .

We consecutively perform two HVs minimizing the SSE assuming the same training and validation samples: the first HV sequentially optimizes the single-scale processes  $z_1(s_i), \dots, z_R(s_i)$

along with the terminal resolution  $R$ , and the second HV refines these processes to mitigate potential bias introduced by the first HV that prioritizes large-scale processes. Section 4.2.1 and 4.2.2 describe the two HVs.

#### 4.2.1. First HV optimizing the terminal resolution $R$

This step simultaneously optimizes  $\boldsymbol{\beta}$  and the predictive mean  $\hat{z}_{1:R}(s_i)$ . The optimization procedure iteratively fits single-scale spatial processes while gradually reducing the bandwidth as follows (see Figure 5):

- (1) Initialize  $R = 1$ ,  $\hat{z}_{1:R}(s_i) = \hat{z}_R(s_i) = 0$ ,  $SSE_R = \infty$ , and  $h_R$  by a sufficiently long distance.
- (2) Evaluate the ordinary least squares (OLS) estimator  $\hat{\boldsymbol{\beta}} = (\mathbf{X}'\mathbf{X})^{-1}\mathbf{X}'(\mathbf{y} - \hat{\mathbf{z}}_{1:R})$ , where  $\mathbf{y}$  is a vector of explained variables,  $\mathbf{X}$  is a matrix of covariates, and  $\hat{\mathbf{z}}_{1:R} = [\hat{z}_{1:R}(s_1), \dots, \hat{z}_{1:R}(s_N)]'$ .

Update the residual as  $\hat{e}_{R+1}(s_i) = y(s_i) - \mathbf{x}(s_i)'\hat{\boldsymbol{\beta}} - \hat{z}_{1:R}(s_i)$ .

- (3) Fit LAMP for the residuals as  $\hat{e}_{R+1}(s_i) \sim N(\hat{z}_{R+1}(s_i), \sigma_{R+1}^2(s_i))$  following Section 3. In other words, distribute and fit  $C_R$  local models for the residuals and evaluate the aggregated predictive mean  $\hat{z}_{R+1}(s_i)$  and variance  $\sigma_{R+1}^2(s_i)$  using Eqs. (9 - 10).

- (4) Evaluate  $SSE_{R+1} = \sum_{i_v=1}^{N_v} \left( y(s_{i_v}) - \mathbf{x}(s_{i_v})'\hat{\boldsymbol{\beta}} - \hat{z}_{1:R}(s_{i_v}) - \hat{z}_{R+1}(s_{i_v}) \right)^2$ :

- (a) If  $SSE_{R+1} < SSE_R$ , update the process  $\hat{z}_{1:R+1}(s_i) = \hat{z}_{1:R}(s_i) + \hat{z}_{R+1}(s_i)$ , reset counter  $Q = 0$ , and go to step (5).

(b) Otherwise,  $Q \rightarrow Q + 1$ . If  $Q$  is less than a threshold value, which is 5 in our case, go to step

(5). Otherwise,  $R$  is the optimal terminal resolution, and  $\hat{\boldsymbol{\beta}}$  and  $\hat{z}_{1:R}(s_i)$  are the primal outputs.

(5) Increase resolution  $R \rightarrow R + 1$ , reduce bandwidth  $h_{R+1} = \delta h_R$ , where we assumed  $\delta = 0.9$ , and go back to step (2).

In step (3), the variance  $\tau_{c_{R+1}}^2$  of the Gaussian prior  $\mu_{c_{R+1}} \sim N(0, \tau_{c_{R+1}}^2)$  is approximated by the sample variance of  $\hat{\mu}_{c_R}$  estimated in the previous iteration, under the assumption that the variance explained at resolution  $R + 1$  is roughly the same as at resolution  $R$ . The assumption is acceptable as long as the gap between  $h_{R+1}$  and  $h_R$  is small.  $\text{Var}[\hat{\boldsymbol{\beta}}]$  may be evaluated in the OLS step to evaluate statistical significance of the coefficient.

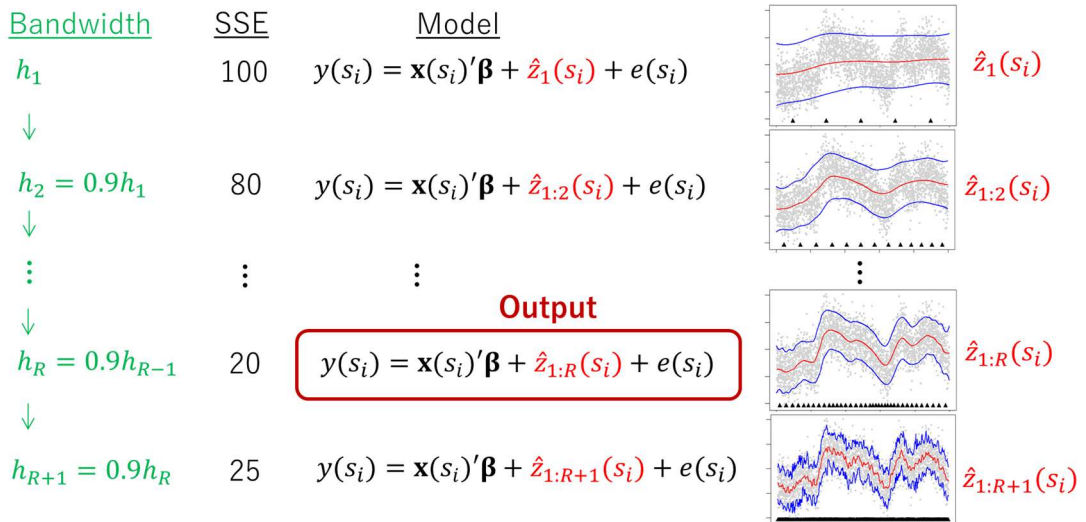


Figure 5: The first hold validation procedure. The bandwidth value is gradually reduced assuming the discount ratio  $\delta = 0.9$  until the validation SSE does not improve any more.

#### 4.2.2. Second HV optimizing the adjustment parameters

Although the first HV optimizes  $\hat{z}_1(s_1), \dots, \hat{z}_R(s_N)$  to minimize  $SSE_R = \sum_{i_v=1}^{N_v} (y(s_{i_v}) - \mathbf{x}(s_{i_v})' \hat{\boldsymbol{\beta}} - \hat{z}_{1:R}(s_{i_v}))^2$ , the solution would be sub-optimal because they are optimized not simultaneously but sequentially according to scale  $r$ .

Therefore, we replace the estimate  $\hat{z}_r(s_i)$  with an adjusted estimate  $\hat{z}_r^*(s_i) = \alpha_r \hat{z}_r(s_i)$  reducing  $SSE_R$ . To reduce bias associated with scale or bandwidth  $h_r$ , the adjustment parameter is specified as  $\alpha_r = \theta_1 \exp(-\theta_2 h_r)$ . The parameters  $\theta_1$  and  $\theta_2$  are optimized through HV minimizing  $SSE_R^* = \sum_{i_v=1}^{N_v} (y(s_{i_v}) - \mathbf{x}(s_{i_v})' \hat{\boldsymbol{\beta}} - \sum_{r=1}^R \hat{z}_r^*(s_{i_v}))^2$ . If  $\hat{\theta}_1 = 1$  and  $\hat{\theta}_2 \rightarrow 0$ , the  $\alpha_r$  parameter becomes uniformly one making no adjustment. Otherwise, the second HV reduces the validation error.

#### 4.3. Non-linear LAMP model

This section considers the LAMP model (Eq. 11) considering the non-linear term  $f(\mathbf{x}_f(s_i))$ . As an example, a random forest model is assumed for  $f(\mathbf{x}_f(s_i))$ . As explained in Section 4.1, we optimize the non-linear term after estimating the other simpler terms. The procedure is as follows:

- (1) Apply the first and second HVs and obtain the optimal predictor  $\hat{y}_R^*(s_i) = \sum_{k=1}^K x_k(s_i) \hat{\beta}_k + \sum_{r=1}^R \hat{z}_r^*(s_i)$  as detailed in Section 4.2,

(2) Optimize the  $f(\mathbf{x}_f(s_i))$  function by another HV minimizing the SSE of the predictor  $\hat{y}_R^{**}(s_i) =$

$\hat{y}_R^*(s_i) + f(\mathbf{x}_f(s_i))$  using the same training and validation samples.

(3) If SSE reduces,  $\hat{y}_R^{**}(s_i)$  is the output predictor, otherwise,  $\hat{y}_R^*(s_i)$  is the output.

Since step (2) is just the conventional HV, it is easily implemented using off-the-shelf software packages. In other words, neural networks, random forest, and other functions are available for  $f(\mathbf{x}_f(s_i))$ . This simple algorithm is useful to estimate highly sophisticated models considering linear and non-linear trends as well as latent spatial processes.

#### 4.4. Uncertainty modeling

The first HV estimates the distribution of  $z_r(s_i) \sim N(\hat{z}_r(s_i), \sigma_r^2(s_i))$  for  $r \in \{1, \dots, R\}$ ,

comprised of  $z_{1:R}^*(s_i) = \sum_{r=1}^R z_r^*(s_i)$ . Using this property, the predictive values of our model can be resampled efficiently. In case of the linear LAMP model (Eq. 12), the  $b$ -th resamples are obtained as follows:

(1) Resample  $\boldsymbol{\beta}^{(b)} \sim N(\hat{\boldsymbol{\beta}}, \text{Var}[\hat{\boldsymbol{\beta}}])$ .

(2) Resample  $z_r^{(b)}(s_i) \sim N(\hat{z}_r(s_i), \sigma_r^2(s_i))$  for each  $r$  and evaluate  $z_{1:R}^{*(b)}(s_i) = \sum_{r=1}^R \alpha_r z_r^{(b)}(s_i)$ .<sup>2</sup>

(3) Resample  $e_R^{(b)}(s_i)$  from  $\hat{e}_R(s_1), \dots, \hat{e}_R(s_N)$  with replacement.<sup>3</sup>

---

<sup>2</sup> The adjustment parameters  $\hat{\theta}_1, \hat{\theta}_2$  in  $\hat{\alpha}_{\hat{\theta}_r}$  are fixed by their estimates since our preliminary analysis suggested that their uncertainty is small and little impact on the analysis result.

<sup>3</sup> The residuals  $\hat{e}_R(s_1), \dots, \hat{e}_R(s_N)$  would be nearly independent and exchangeable since spatial dependence is filtered by the spatial process term  $z_{1:R}^*(s_i)$  (see, Murakami and Griffith, 2015)

(4) Simulate the predictive value as  $y^{(b)}(s_i) = \mathbf{x}'(s_i)\boldsymbol{\beta}^{(b)} + z_{1:R}^{*(b)}(s_i) + e_R^{(b)}(s_i)$ .

In case of the non-linear LAMP model, step (4) is replaced with steps (5) and (6):

(5) Resample  $f(\mathbf{x}_f(s_i))^{(b)}$  from the trained model.

(6) Simulate the predictive value as  $y^{(b)}(s_i) = \mathbf{x}'(s_i)\boldsymbol{\beta}^{(b)} + f(\mathbf{x}_f(s_i))^{(b)} + z_{1:R}^{*(b)}(s_i) + e_R^{(b)}(s_i)$ .

For example, if  $f(\mathbf{x}_f(s_i))^{(b)}$  is a random forest model, quantile regression forests (Meinshausen and Ridgeway, 2006) is available in step (5). By iterating the simulation  $B$  times (e.g.,  $B = 200$ ), the replicates  $y^{(1)}(s_i), \dots, y^{(B)}(s_i)$  are useful to evaluate predictive variance, interval, and other uncertainty measures.

#### 4.5. Properties

LAMP differs from existing spatial process models in several aspects. First, whereas spatial dependence is typically modeled through covariance functions, LAMP relies on local weighting. A related approach is GWR, in which the estimated local coefficients are directly interpreted. In contrast, LAMP takes a multiscale ensemble of local models to construct a spatial process, and can thus be regarded as an extension of GWR. To date, little attention has been paid to such locally weighted stochastic processes in spatial statistics, making LAMP a distinctive contribution.

Second, LAMP does not require explicit matrix inversion, a computational bottleneck in conventional spatial models, particularly GPs. In addition, within each scale, the local models are

estimated independently, making this step readily parallelizable. Thus, LAMP offers a computationally efficient alternative for spatial process modeling.

Third, LAMP is optimized using HV, in contrast to the likelihood-based inference that is commonly adopted in spatial statistics. Because many machine learning algorithms are also optimized via validation, HV provides a natural basis for integrating LAMP with these algorithms.

Thus, our proposed LAMP is unique, scalable, and machine-learning-compatible spatial process. Section 5 investigates this predictive performance through Monte Carlo experiments.

## 5. Monte Carlo experiment

Section 5.1 presents a Monte Carlo experiment for comparing our linear LAMP with alternative models, while Section 5.2 reports a similar experiment for the non-linear LAMP, taking random forest as a representative example.

### 5.1. Experiment for the linear LAMP model

#### 5.1.1. Outline

This section evaluates the predictive accuracy of our method using synthetic samples generated from the following model:

$$y(s_i) = \beta_0 + \beta_1 x_1(s_i) + \beta_2 x_2(s_i) + z(s_i) + e(s_i), \quad e(s_i) \sim N(0,1), \quad (13)$$

$$z(s_i) = \sum_{j=1}^N w_h^{scale}(d_{ij}) u_k(s_j), \quad u_k(s_i) \sim N(0,2^2)$$

where  $\{\beta_0, \beta_1, \beta_2\} = \{1, 2, -0.5\}$  and  $w_h^{scale}(d_{ij}) = \frac{w_h(d_{ij})}{\sum_j w_h(d_{ij})}$  is a row-standardized weight where  $w_h(d_{ij}) = \exp(-d_{ij}/h)$ . Spatial coordinates of the data  $y(s_i)$  are randomly selected within the region  $[0, 10] \times [0, 10]$ . Since most data are spatially correlated in many real-world cases, spatial processes were also assumed in the covariables as follows:

$$x_k(s_i) = 0.5z_k(s_i) + 0.5e_k(s_i), \quad e_k(s_i) \sim N(0,1), \quad (14)$$

$$z_k(s_i) = \sum_{j=1}^N w_1^{scale}(d_{ij}) u_k(s_j), \quad u_k(s_i) \sim N(0,1).$$

The synthetic data is generated 200 times for each case with different training sample sizes  $N \in \{500, 1000, 2000, 3000, 6000, 12000, 20000\}$  and bandwidths  $h \in \{0.2, 1.0\}$ . As illustrated in Figure 6, the spatial process  $z(s_i)$  has small-scale variations when  $h = 0.2$  while large-scale variations when  $h = 1.0$ . The two cases are useful to examine how accurately the algorithm estimates the scale of the process.

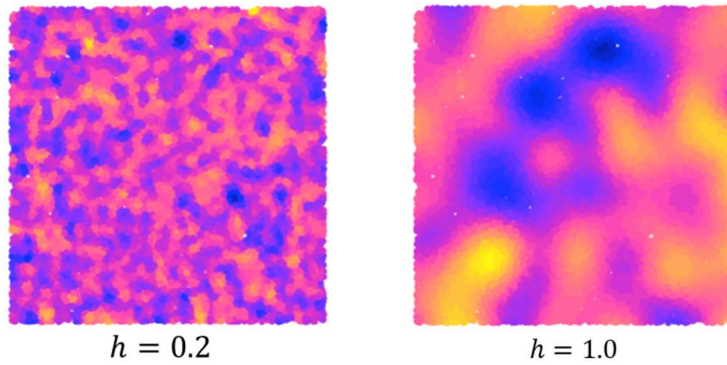


Figure 6: Spatial process  $z(s_i)$  simulated with  $h \in \{0.2, 1.0\}$ .

In each trial, 1,000 test samples are additionally generated in the study region, and used to evaluate the predictive root mean squared error (RMSE) and mean absolute error:

$$RMSE = \sqrt{\frac{1}{N} \sum_{i=1}^N (y(s_i) - \hat{y}(s_i))^2}, \quad (15)$$

$$MAE = \frac{1}{N} \sum_{i=1}^N |y(s_i) - \hat{y}(s_i)|. \quad (16)$$

RMSE and MAE measure the accuracy of predictive value itself. RMSE is more sensitive to outliers due to squaring, while MAE treats all errors equally. The RMSE and MAE values of the linear LAMP model (LAMP) are compared with the conventional spatial GP (GP) as well as popular scalable alternatives including low rank GP (LGP; see, Wood, 2017), conjugate NNGP whose variance and bandwidth parameters are optimized by 5-fold cross-validation (Finley et al., 2019), and the SPDE method<sup>4</sup> (see Section 1).

GP is optimized through the non-linear weighted least squares estimation (Cressie, 2015), which is implemented in an R package `gstat` (<https://cran.r-project.org/web/packages/gstat/index.html>). Considering computational complexity, we apply GP only in cases with  $N \leq 3000$ . LGP is implemented using an R package `mgcv` (<https://cran.r-project.org/web/packages/mgcv/index.html>), and the number of basis functions follow the default setting in the package. NNGP and SPDE are

---

<sup>4</sup> The maximum edge length of the spatial graph used to approximate GP was set to 0.25, which is considered sufficiently small relative to the size of the study region  $[0, 10] \times [0, 10]$ .

implemented by the spNNGP (<https://cran.r-project.org/web/packages/spNNGP/index.html>) and INLA (<https://www.r-inla.org/home>) packages, respectively.

### 5.1.2. Result

Figure 7 displays the medians of the RMSE and MAE values. When the true process has large-scale pattern with  $h = 1.0$ , GP performs the best as expected. SPDE and LAMP indicated similar performance for  $N \leq 3000$ , and the smallest RMSE and MAE values for  $3000 < N$ . The accuracy of the proposed method is confirmed for large-scale spatial modeling.

In case of small-scale process with  $h = 0.2$ , GP fails to capture local patterns, and the resulting process was less accurate. This might be due to the difficulty in distinguishing small-scale variation in  $z(s_i)$  and noise in  $e(s_i)$ . On the other hand, NNGP accurately predicted the small-scale pattern. Because NNGP is a nearest-neighbor-based approximation, the result is reasonable. LAMP indicated even smaller errors owing to the sequential learning procedure optimizing the scale. As shown in Figure 7, only LAMP achieved accurate prediction for both the large-scale and small-scale processes.

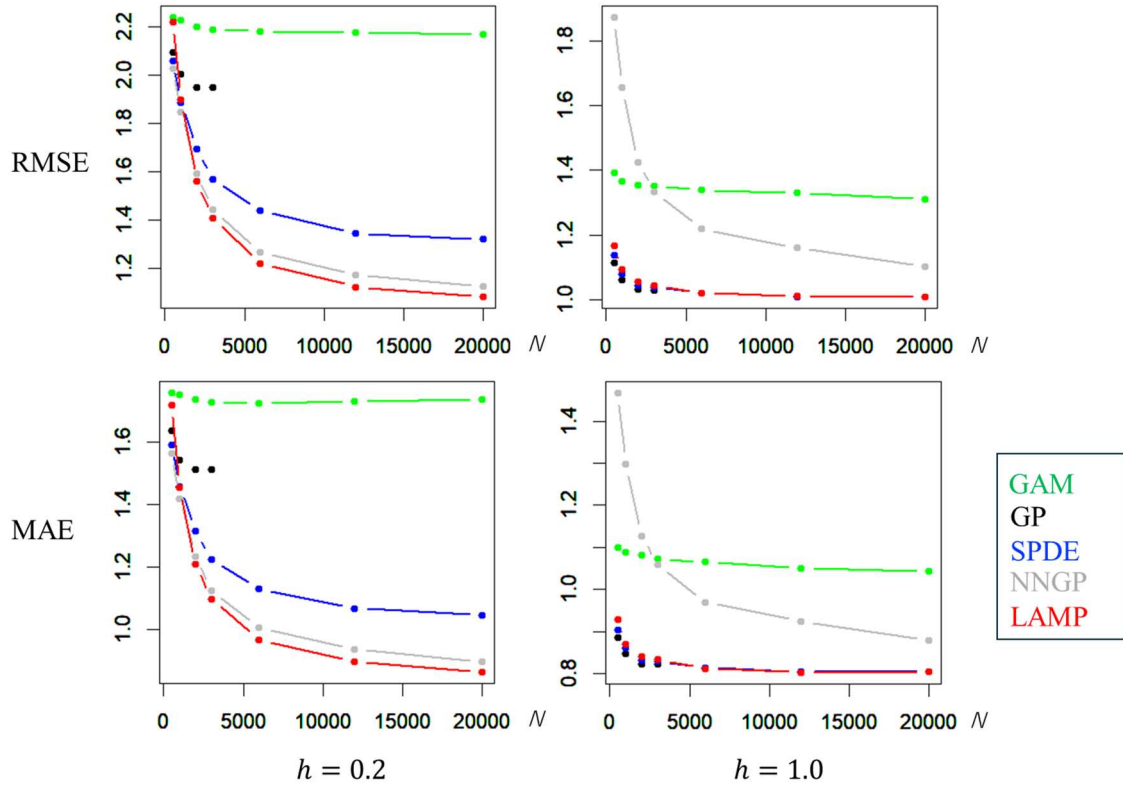


Figure 7: Medians of the RMSE and MAE values (True: linear spatial model).

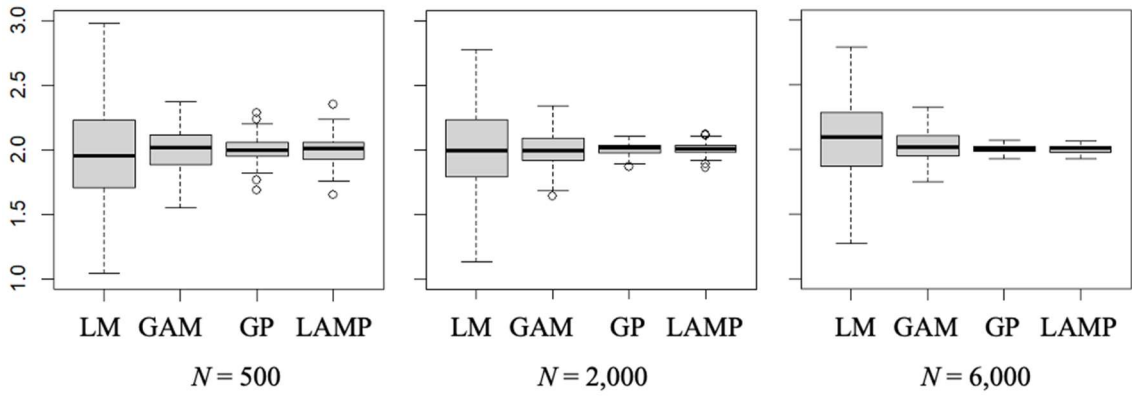


Figure 8: Boxplots of the estimated  $\hat{\beta}_1$  values (true:  $\beta_1 = 2.0$ ) for  $N = 500, 2,000,$  and  $6,000$ .

Figure 8 compares the boxplots of the estimated values of the regression coefficient  $\beta_1$ .

Results for  $\beta_2$ , which were similar to those for  $\beta_1$ , are omitted for simplicity. Here, LAMP is

compared with GAM and GP, which are widely used for regression analysis, as well as the basic linear regression (LM). Due to the ignorance of spatial dependence which results in the loss of statistical efficiency (LeSage and Pace, 2009), the coefficient estimates of LM varied considerably across trials and are less accurate. The coefficient estimates of GAM were also less accurate because of the low predictive model accuracy reported in Figure 8. By contrast, the estimates of LAMP consistently remain close to the true value of  $\beta_1 = 2.0$  similar to GP. This result highlights the usefulness of LAMP for an accurate coefficient estimation.

Figure 9 compares median computation times over five iterations. All computations were performed in R 4.5.1 on a Windows 11 Pro with a 13th Gen Intel Core i7-13700 CPU and 16 GB of memory. The computation time of GP rapidly increased with  $N$  as expected. In contrast, the computation time of LAMP was much shorter, and increases only linearly with respect to  $N$ , confirming its computational efficiency. For example, for  $N = 12,000$ , GP took 225.7 seconds on average while LAMP took only 7.4 seconds. Still, it was slower than SPDE, NNGP, and GAM. Parallelization of LAMP might be required for very large samples.

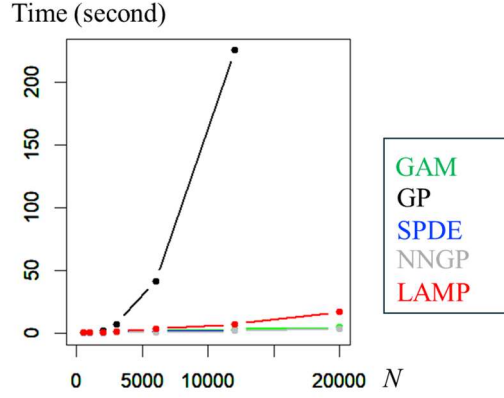


Figure 9: Median computation time. GP was not estimated when  $N = 20,000$  due to a memory limit.

## 5.2. Experiment for the non-linear LAMP model

### 5.2.1. Outline

To evaluate the performance of the non-linear LAMP model, we generated simulation samples according to

$$y(s_i) = \beta_0 + \beta_1 \exp(x_1(s_i)) + \beta_2 x_2^+(s_i) + z(s_i) + e(s_i), \quad e(s_i) \sim N(0,1), \quad (17)$$

where  $x_2^+(s_i) = \max(x_2(s_i), 0)$ . The covariates  $x_1(s_i), x_2(s_i)$  and the spatial process  $z(s_i)$  are generated in the same manner as in the previous section. We set  $\beta_0 = 1$ , and choose  $\beta_1$  and  $\beta_2$  such that  $\text{Var}[\beta_1 \exp(x_1(s_i))] = \text{Var}[\beta_2 x_2^+(s_i)] = 2^2$ , which equals  $\text{Var}[z(s_i)]$ . Because of the non-linear effects from  $x_1(s_i)$  and  $x_2(s_i)$ , the non-linear LAMP model is appropriate in this case.

The samples are generated 200 times for each case with  $N \in \{500, 1000, 2000, 3000, 6000, 12000, 20000\}$  and kernel bandwidth  $h = 1.0$ . In each case, RMSE and MAE of the following models are compared: the linear LAMP (LAMP), the non-linear LAMP

with additional training by the random forest (LAMP-RF), random forest (RF) based on 5 fold cross-validation, implemented in the ranger (<https://cran.r-project.org/web/packages/ranger/index.html>) R package, and the SPDE approach, which was found to be accurate in case of  $h = 1.0$  in the previous section. In RF and the RF training part of LAMP-RF, spatial coordinates are considered as additional covariates to capture spatial patterns. Among the RF hyperparameters, the number of candidate predictors at each split and the minimum number of samples per terminal node can strongly influence on analysis result. They are optimized through grid search, while the number of trees is fixed at 500, since results were found to be similar when this was increased.

### 5.2.2. Predictive accuracy

Figure 10 compares predictive accuracy. As expected, SPDE and LAMP, which are linear models, failed to capture non-linearity and thus showed lower accuracy. In contrast, RF, which can model non-linearity, tended to be more accurate. Our LAMP-RF achieved the lowest RMSE and MAE values across cases, demonstrating its superior predictive accuracy.

Table 1 compares the accuracy of the four models for predicting the data generated from the linear model (Eqs. 15-16) with  $h = 1.0$ . RF performed poorly because it failed to exploit the underlying linearity. In contrast, LAMP-RF produced the same results as LAMP, confirming its accuracy. These results confirm the predictive accuracy of LAMP-RF for in linear and non-linear cases.

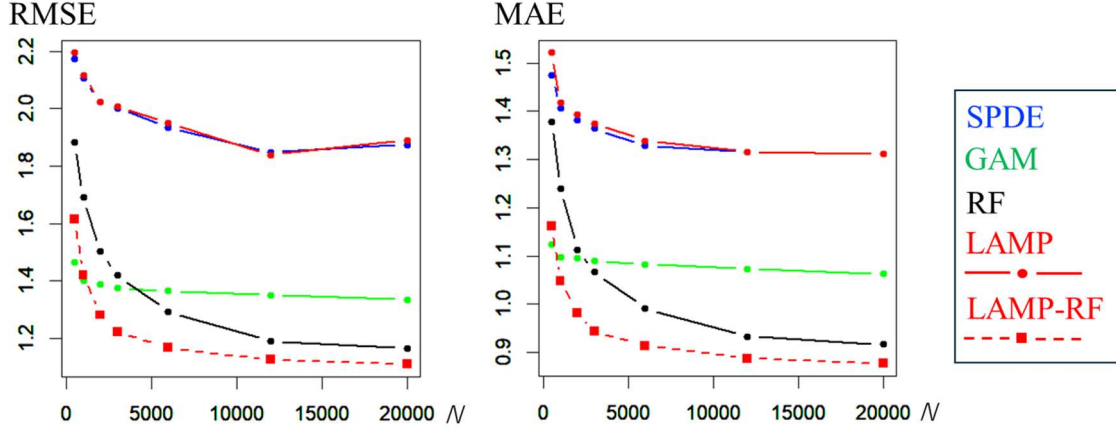


Figure 10: Medians of the RMSE (left) and MAE (right) values (True: non-linear spatial model).

Table 1: Medians of the RMSE and MAE values (True: linear spatial model with  $N=6,000$ ).

	SPDE	GAM	RF	LAMP	LAMP-RF
RMSE	1.020	1.331	1.184	1.020	1.020
MAE	0.814	1.064	0.941	0.812	0.812

### 5.2.3. Partial dependence of the covariates

Figure 11 presents the accumulated local effects (ALE) plots showing the average effects of  $x_1(s_i)$  and  $x_2(s_i)$  on the model's predictions (Apley and Zhu, 2020). As summarized in Table 2, LAMP-RF estimated the non-linear effect  $f(x_1(s_i)) = \beta_1 \exp(x_1(s_i))$  more accurately than RF, likely because the pre-trained linear trend helps capture the rapid increase of  $f(x_1(s_i))$  for large  $x_1(s_i)$  values (Figure 11 (left)). In contrast, LAMP-RF showed lower accuracy for  $f(x_2(s_i)) =$

$\beta_2 x_2^+(s_i)$ , as the pre-trained negative linear trend leads to underestimation for large  $x_2(s_i)$  values (e.g., Figure 11 (right)). Thus, near the edges of the ALE plot, such pre-trained linear trends can distort nonlinear patterns due to limited samples, which make it difficult to adjust to the true (non-linear) trend. Nevertheless, the overall estimation results of LAMP-RF are close to those of conventional RF and remain similarly interpretable.

To mitigate the abovementioned edge effects in the ALE plots, the plots may be interpreted only within the 95 % percentile interval (see Figure 11). A more promising direction for future work is to relax the linear pretraining in LAMP-RF to better capture nonlinear trends, for example by incorporating spline-based models.

In summary, the linear LAMP and non-linear LAMP (LAMP-RF) provide highly accurate prediction and coefficients estimates, as well as interpretable non-linear effects in case of LAMP-RF.

The next section illustrates their practical utility through an empirical application.

Table 2: Medians of the RMSE and MAE values (True: linear spatial model with  $N=6,000$ ).

	$f(x_1(s_i))$		$f(x_2(s_i))$	
	RF	LAMP-RF	RF	LAMP-RF
RMSE	2.452	2.181	0.347	0.376
MAE	0.370	0.363	0.184	0.232

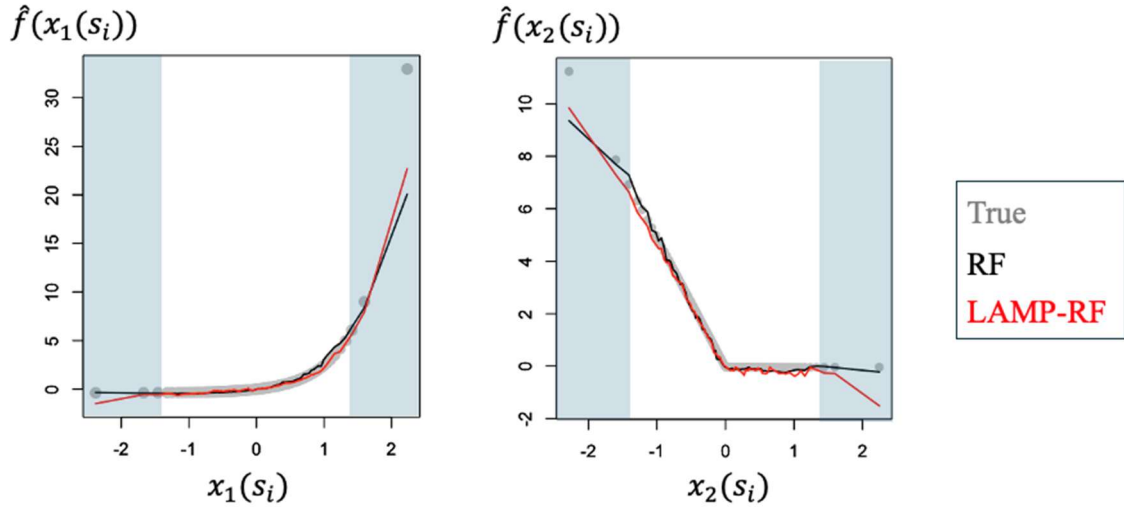


Figure 11: Example of estimated non-linear effects of  $x_1(s_i)$  and  $x_2(s_i)$  ( $N=6,000$ ). Regions outside the 95 % percentile interval are down in blue.

## 6. Application

### 6.1. Outline

This section applies the proposed method to an analysis of residential land prices in 2007 in the Tokyo metropolitan area. The explained variable is the log-transformed residential land price ( $N = 7,497$ ; JPY/m<sup>2</sup>). As shown in Figure 12, land prices tend to be high in central Tokyo. The study area has a well-developed railway network, and many residents commute to the center by train. As a result, high price areas stretch along train lines.

The models compared are linear regression (LM), random forest (RF), GP based on Gaussian and exponential kernels ( $GP_{\text{Gau}}$ ,  $GP_{\text{Exp}}$ ), LAMP based on these kernels ( $LAMP_{\text{Gau}}$ ,  $LAMP_{\text{Exp}}$ ), and LAMP additionally trained by RF ( $LAMP\text{-}RF_{\text{Gau}}$ ,  $LAMP\text{-}RF_{\text{Exp}}$ ).

Their covariables are the Euclidean distance from the nearest railway station (StaDist; km), railway network distance from the nearest station to Tokyo station (TokyoDist; km), and each of the proportion of agricultural land, forest, wasteland, and river in the 500 m grid including the sample site (Agri, Forest, Waste, River). In addition, for RF, longitude and latitude are also considered as covariables to learn spatial patterns. Data of the land priced and covariates are available from National Land Numerical Information download site (<https://nlftp.mlit.go.jp/ksj/>).

The models are used to predict land price in each district called *Cho-Cho-Aza*, whose spatial coordinates are given by their geometric center.

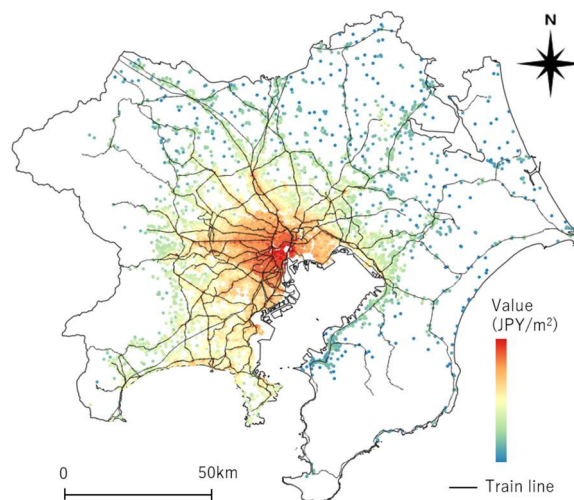


Figure 12: Residential land price in the Tokyo metropolitan area. Central Tokyo, shown at the center of this map, records highest land prices.

## 6.2. Parameter estimation results

Table 3 summarizes the estimated parameters of the linear models. All models indicate statistically significant negative effects of TokyoDist and StationDist, reflecting higher land prices near Tokyo station and other train stations. The coefficients for Agri, Forest, Waste, and River are also negative, suggesting that these non-urban land uses are less attractive than urban land uses that provide urban facilities. These results are intuitively consistent.

The coefficients estimated by LAMP are similar to those obtained by GP, with substantially smaller absolute values for Agri, Waste, and River compared to LM. This implies that LAMP offers a reasonable alternative to GP for reducing residual spatial dependence and improving the accuracy of coefficient estimation. Furthermore, the standard errors of the LAMP coefficients are generally smaller than those of GP, consistent with its improved accuracy as indicated by the lower residual standard error.

Notably, the standard deviation of the estimated spatial process in LAMP is comparable to that of GP, indicating that LAMP attains higher accuracy without incurring variance inflation or overfitting. This improvement stems from its flexibility in modeling multi-scale processes, in contrast to GP, which assumes a single scale with an estimated bandwidth of 48.98 km. The optimal number of resolutions in LAMP is 40, with the bandwidths ranging from 77.03 km to 1.27 km, suggesting the multi-scale structure underlying the land price distribution.

Table 3: Parameter estimates (linear models). SE and SD stand for standard error and standard deviation, respectively. Spatial SD represents the standard deviation of the spatial process. Regarding GP, the estimated noise variance (i.e., nugget) is displayed in the “Residual SD” row.

Coefficients	LM		GP		LAMP	
	Estimate	SE	Estimate	SE	Estimate	SE
Const	13.317	$1.13 \times 10^{-2}$ ***	13.20	$2.81 \times 10^{-1}$ ***	13.30	$3.84 \times 10^{-3}$ ***
TokyoDist	-0.026	$3.12 \times 10^{-4}$ ***	-0.019	$1.82 \times 10^{-2}$ ***	-0.028	$1.10 \times 10^{-4}$ ***
StationDist	-0.096	$3.79 \times 10^{-3}$ ***	-0.136	$4.52 \times 10^{-3}$ ***	-0.129	$1.14 \times 10^{-3}$ ***
Agri	-1.455	$3.80 \times 10^{-2}$ ***	-0.697	$2.84 \times 10^{-2}$ ***	-0.603	$1.33 \times 10^{-2}$ ***
Forest	-0.557	$5.50 \times 10^{-2}$ ***	-0.485	$4.19 \times 10^{-2}$ ***	-0.432	$1.88 \times 10^{-2}$ ***
Waste	-2.287	$2.66 \times 10^{-1}$ ***	-0.283	$1.74 \times 10^{-1}$ *	-0.214	$9.15 \times 10^{-2}$ **
River	-0.767	$6.96 \times 10^{-2}$ ***	-0.345	$4.56 \times 10^{-1}$ ***	-0.316	$2.35 \times 10^{-2}$ ***
Residual SD	0.471		0.257		0.156	
Spatial SD	0.000		0.504		0.497	
Bandwidth			48.98		1.27 - 77.03	
Resolution					40	

1):\*, \*\*, \*\*\* indicate statistical significance of 10 %, 5 %, and 1 %, respectively.

The estimated 40 scale-wise processes are summed to form the large-scale ( $b_r \geq 30$ ), medium-scale ( $30 > b_r \geq 10$ ), and small-scale ( $10 > b_r$ ) components, as shown in Figure 13. The large-scale process exhibits high values in the south-western area. Historically, this region benefited from the early expansion of railway networks, which improved accessibility and accelerated suburbanization. With the inflow of affluent households and the development of high-quality residential environments, including educational and cultural facilities, the south-west gradually

emerged as a prestigious residential zone. The large-scale pattern likely reflects such a tendency. The medium-scale process shows high values in the outer mountainous areas, possibly reflecting the premium for natural amenities not represented by the covariates. Around central Tokyo, both the medium- and small-scale processes exhibit high values, suggesting that Tokyo influences its neighboring area at multiple spatial scales. By contrast, many other cities show peaks only in the small-scale process. These include prefectural capitals, including Yokohama, Saitama, and Chiba, high-end residential areas including Kichijoji, Kunitachi, and Jiyugaoka, and suburban central cities including Kashiwa and Kawagoe (see Figure13). This indicates that these cities have attractiveness not captured by the covariates.

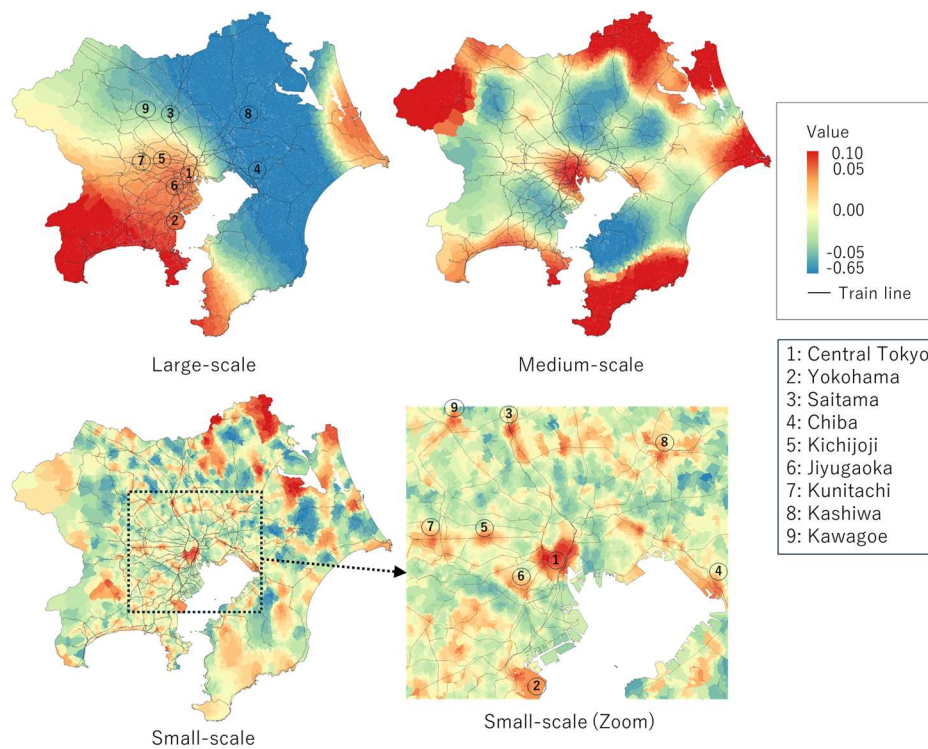


Figure 13: Large-, medium-, and small-scale processes.

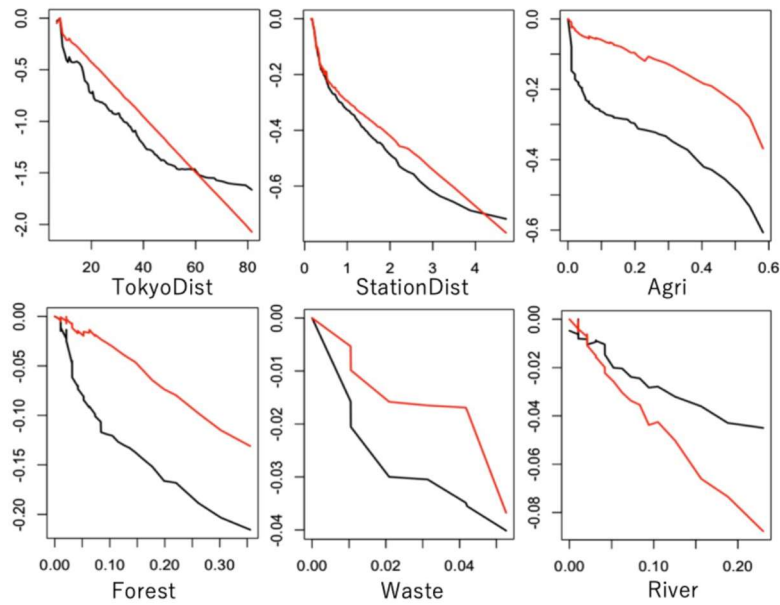


Figure 14: ALE plots (black: RF; red: LAMP-RF). Based on Section 5.2.3, ALEs within the 95 % percentile interval are displayed.

Regarding RF and LAMP-RF, Figure 14 presents the ALEs that measure the partial dependence of each covariate on the logged land prices. Both RF and LAMP-RF reveal a rapid decline of logged land prices near railway stations, with a slower decline further away, indicating a strong preference for areas nearby stations. For TokyoDist, LAMP-RF indicates a linear decline on the log scale, whereas RF suggests a nonlinear decay, implying relatively higher prices in areas far from Tokyo Station, including outer mountainous regions. In LAMP-RF, the higher in mountain areas are absorbed by the medium-scale residual spatial process, which may be interpretable as premium in these areas owing to natural resources (see Figure 13). Overall, the effects estimated by LAMP-RF

tend to be weaker than those from RF, likely because LAMP-RF explicitly models residual spatial dependence, thereby reducing omitted-variable bias.

### 6.3. Spatial prediction result

10-fold cross validation is performed to evaluate RMSE and MAE of the predictive values.

In addition, continuously ranked probability score (CRPS; Gneiting et al., 2005) is also evaluated:

$$CRPS = \int_{-\infty}^{\infty} [F(v) - I(y(s_i) \leq v)] dv, \quad (20)$$

where  $I(y(s_i) \leq v)$  takes 1 if  $y(s_i) \leq v$ , and 0 otherwise. CRPS measures the accuracy of the predictive distribution using the cumulative distribution function  $F(\cdot)$  of the predictive distribution.

Table 4 summarizes the cross-validation results. It indicates that LAMP and LAMP-RF models outperform LM, RF, and GPs in terms of RMSE and MAE, with high predictive mean accuracies. The gap between  $LAMP(-RF)_{Gau}$  and  $LAMP(-RF)_{Exp}$  is smaller than the gap between  $GP_{Gau}$  and  $GP_{Exp}$  suggesting that the proposed methods are robust to the choice of kernel function. LAMP(-RF) has small CRPS values suggesting that method is able to accurately model predictive means as well predictive distributions. In addition, LAMP-RF was found to have smaller errors than LAMP for both the kernels, indicating that the additional learning improved predictive accuracy.

Henceforth, we focus on the exponential kernel-based specifications based on the comparison results.

Table 4: Cross-validation result (Bold: best and second-best models).

Model	RMSE	MAE	CRPS
LM	40.889	0.356	0.349
RF	19.080	0.147	0.109
GP <sub>Gau</sub>	20.910	0.169	0.126
LAMP <sub>Gau</sub>	19.345	0.146	0.112
LAMP-RF <sub>Gau</sub>	<b>18.513</b>	<b>0.141</b>	<b>0.108</b>
GP <sub>Exp</sub>	19.098	0.149	0.116
LAMP <sub>Exp</sub>	19.063	0.144	0.110
LAMP-RF <sub>Exp</sub>	<b>18.200</b>	<b>0.137</b>	<b>0.104</b>

Figure 15 maps predicted land prices. The results of GP<sub>Exp</sub>, LAMP<sub>Exp</sub>, and LAMP-RF<sub>Exp</sub> are quite similar. Compared to LM, they indicated higher prices in central Tokyo and its western area, known as popular residential district due to a number of factors including lower disaster risk, better urban infrastructure, and stronger brand image (see Kanno and Shiohama, 2022). In other words, the three models effectively capture the localized price increases in high-end neighborhoods through residual spatial dependence modeling. Compared to RF, they indicated lower land prices in outer mountainous areas whose land price should be lower than the other regions. It might be because RF, which ignores spatial dependence, has difficulty in capturing local features in these areas with limited samples. In summary, the results of GP<sub>Exp</sub>, LAMP<sub>Exp</sub>, and LAMP-RF<sub>Exp</sub> are intuitively more

reasonable than LM and RF, highlighting the importance of modeling spatial processes to predict land prices.

Figure 16 compares the predictive standard deviations, which quantify the uncertainty of the predicted values. For RF, the standard deviations are evaluated following Meinshausen and Ridgeway (2006). LM indicate consistently high standard deviations, indicating its low accuracy due to spatial dependence being ignored. RF exhibits spatially discontinuous patterns for the same reason. In contrast,  $GP_{Exp}$  produces the smoothest map pattern through the spatial process modeling. The predictive standard deviations of  $LAMP_{Exp}$ , and  $LAMP-RF_{Exp}$  are also smooth but exhibit relatively complex patterns because they assume a complex spatial process composed of  $R = 40$  scale-wise processes.

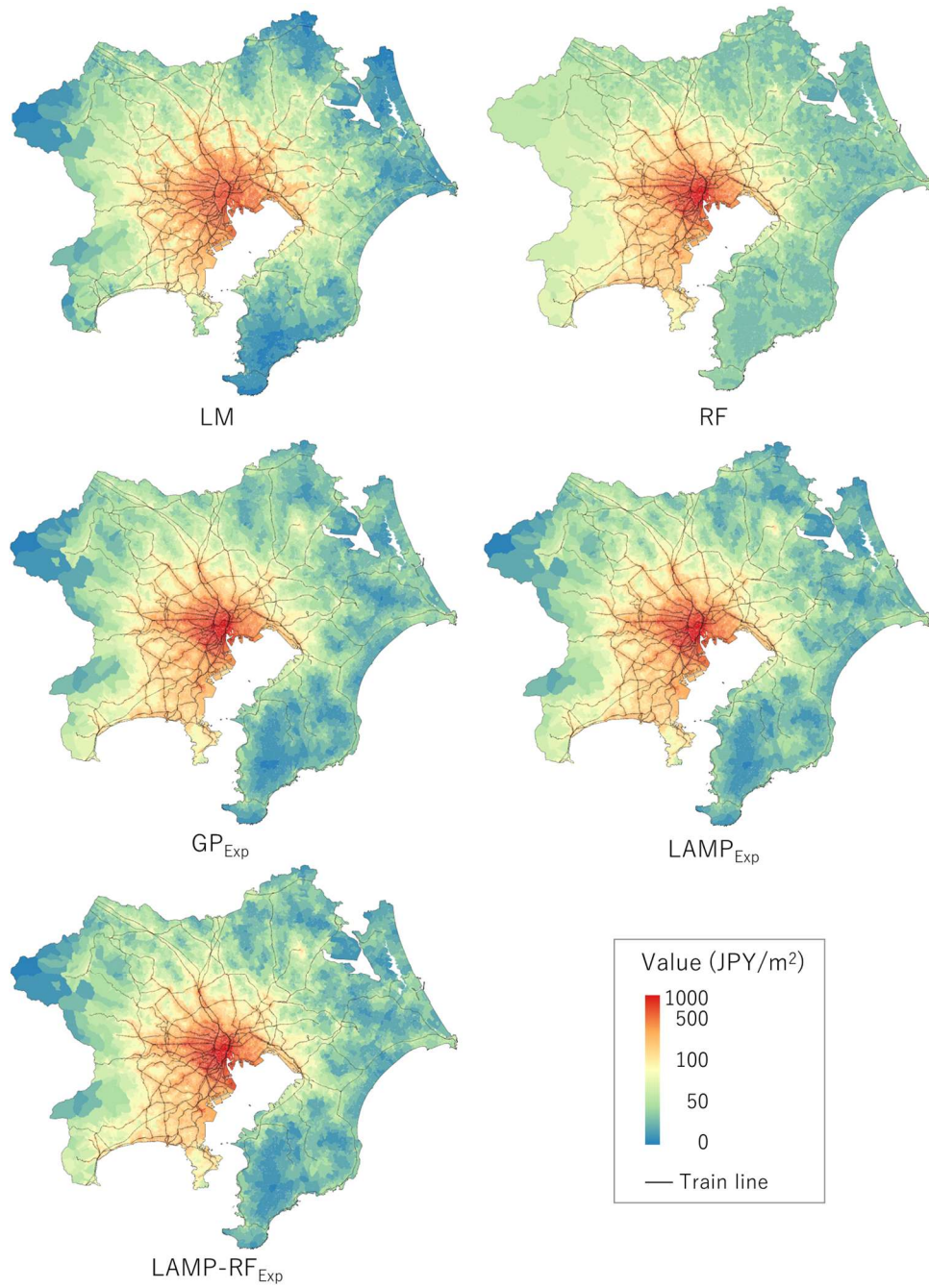


Figure 15: Predicted land prices. Results of  $GP_{Gau}$ ,  $LAMP_{Gau}$ ,  $LAMP-RF_{Gau}$  are omitted for simplicity.

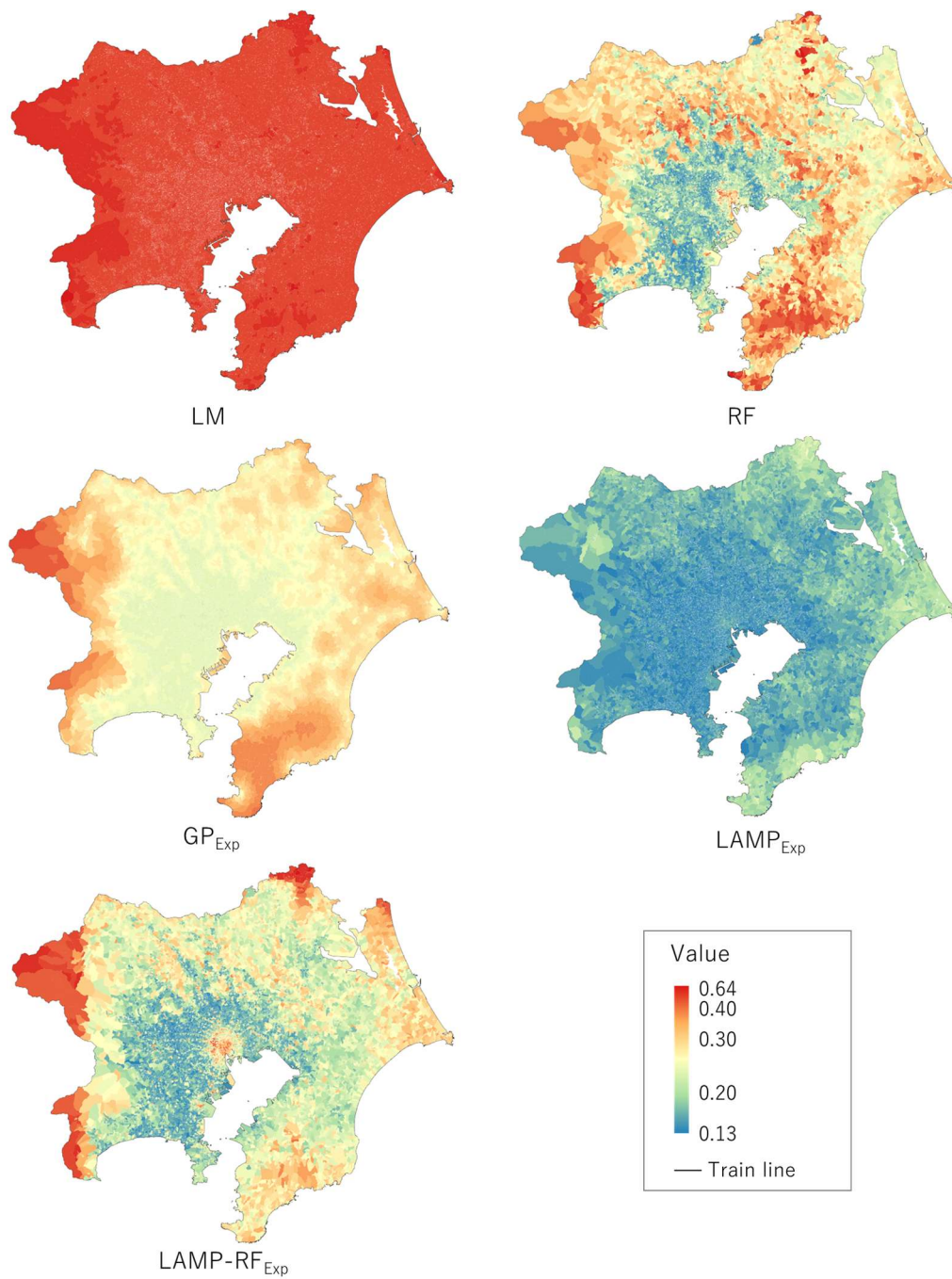


Figure 16: Predictive standard deviations.

Overall, predictive standard deviations tend to be large in peripheral areas with sparse sample sites, as might be expected. In addition, the standard deviations of LAMP<sub>Exp</sub> and LAMP-RF<sub>Exp</sub>

increase in central Tokyo, which is reasonable given this area's complex urban structure, whereas that of  $GP_{Exp}$  decreases. While the map patterns of  $LAMP_{Exp}$  and  $LAMP-RF_{Exp}$  differ from that of  $GP_{Exp}$ , they achieve better accuracy in uncertainty modeling, as indicated by lower CRPS values in Table 2 (recall that CRPS increases either the standard deviations are too small or too large).

## 7. Concluding remarks

This study introduces a novel spatial process, LAMP, together with a sequential learning procedure that trains LAMP alongside linear and non-linear trend functions. Its predictive accuracy and computational efficiency were demonstrated through both simulation experiments and an empirical application. Unlike conventional spatial regression models, LAMP is optimized via holdout validation (HV), which facilitates its integration with machine learning algorithms, as exemplified by the case of RF. In addition, LAMP training is computationally efficient and easily parallelized, highlighting its potential as a fast, accurate, and machine-learning-compatible alternative to conventional likelihood-based spatial process models.

As an initial step to efficiently combine LAMP with machine learning algorithms, the usefulness of such integration should be examined in terms of both modeling accuracy and interpretation while varying samples sizes and the model choices. For instance, integration with GAM is likely to enhance interpretability, whereas integration with neural networks may improve predictive

accuracy in large-scale modeling. These experiments would also help in applying LAMP to other tasks, commonly discussed in the machine learning literature, such as multi-task learning, classification, transfer learning, anomaly detection, and data fusion.

It is also important to extend LAMP itself. Although we assumed spatial processes only for residuals, spatial processes have often been assumed to model spatially varying coefficients (e.g., Gelfand et al., 2003; Comber et al., 2023). Temporal processes, group-wise effects, and other stochastic structures have also been introduced to flexibly model spatio-temporal data (e.g., Wood et al., 2017; Murakami et al., 2025). Extending LAMP to accommodate multiple stochastic processes is therefore an important future direction. In addition, since LAMP does not rely on the assumption of stationarity as spatial GPs do, its efficiency should also be investigated in the context of non-stationary spatial process modeling

A further task is to incorporate loss functions beyond the squared error, such as Poisson loss for count data and logistic loss for binary outcomes. Extending the framework in these directions would enable broader applications of LAMP, including those that remain challenging for conventional spatial statistical models.

The R code for implementing the linear and non-linear LAMP models for spatial prediction is available from [https://github.com/dmuraka/spLAMP\\_dev\\_version/tree/main](https://github.com/dmuraka/spLAMP_dev_version/tree/main).

## Acknowledgements

This work was supported by JSPS KAKENHI Grant Number 24K00175, 25H00546, 25K00624, and 24K00997.

## Reference

- Apley DW, Zhu J (2020) Visualizing the effects of predictor variables in black box supervised learning models. *J R Stat Soc B Stat Methodol* 82: 1059-1086
- Bakka H, Rue H, Fuglstad GA, Riebler A, Bolin D, Illian J, Elias K, Simpson D, Lindgren F (2018) Spatial modeling with R-INLA: A review. *WIREs Comput Stat* 10: e1443.
- Breiman, L. (2001). Random forests. *Mach Learn* 45: 5–32
- Brunsdon C, Fotheringham AS, Charlton ME (1996) Geographically weighted regression: A method for exploring spatial nonstationarity. *Geogr Anal* 28: 281–298
- Cao Y, Fleet DJ (2014) Generalized product of experts for automatic and principled fusion of Gaussian process predictions. *ArXiv* 1410.7827
- Chen W, Li Y, Reich BJ, Sun Y (2020) Deepkriging: Spatially dependent deep neural networks for spatial prediction. *ArXiv* 2007.11972
- Cohen S, Mbuva R, Marwala T, Deisenroth M (2020) Healing products of Gaussian process experts. *Proceedings of the 37th International Conference on Machine Learning: 2068-2077*

- Comber A, Brunsdon C, Charlton M, Dong G, Harris R, Lu B, Lü Y, Murakami D, Nakaya T, Wang Y, Harris P (2023) A route map for successful applications of geographically weighted regression. *Geogr Anal* 55: 155-178
- Cressie N (2015) *Statistics for spatial data*. Wiley, New York
- Cressie N, Shi T, Kang EL (2022) Basis-function models in spatial statistics: Foundations, properties, and extensions. *Stat Sci* 37: 529–553
- Cressie N, Johannesson G (2008) Fixed rank kriging for very large spatial data sets. *J R Stat Soc B Stat Methodol* 70: 209–226
- Datta A, Banerjee S, Finley AO, Gelfand AE (2016) Hierarchical nearest-neighbor Gaussian process models for large geostatistical datasets. *J Am Stat Assoc* 111: 800–812
- Fotheringham AS, Brunsdon C, Charlton M (2009) *Geographically Weighted Regression: The Analysis of Spatially Varying Relationships*. Wiley, New York
- Fotheringham AS, Yang W, Kang W (2017) Multiscale geographically weighted regression (MGWR). *Ann Am Assoc Geogr* 107: 1247–1265
- Friedman JH (2002) Stochastic gradient boosting. *Compute Stat Data Anal* 38: 367–378
- Gelfand AE, Kim HJ, Sirmans CF, Banerjee S (2003) Spatial modeling with spatially varying coefficient processes. *J Am Stat Assoc* 98: 387–396

- Georganos S, Grippa T, Gadiaga, AN, Linard C, Lennert M, Vanhuyse S, Mboga N, Wolff E, Kalogirou S (2021) Geographical random forests: a spatial extension of the random forest algorithm to address spatial heterogeneity in remote sensing and population modelling. *Geocarto Int* 36: 121-136
- Hazra A, Nag P, Yadav R, Sun Y (2025) Exploring the efficacy of statistical and deep learning methods for large spatial datasets: A case study. *J Agric Biol Environ Stat* 30: 231-254
- Heaton MJ, Datta A, Finley AO, Furrer R, Guinness J, Guhaniyogi R, Gerber F, Gramacy RB, Hammerling D, Katzfuss M, Lindgren F, Nychka DW, Sun F, Zammit-Mangion A (2019) A case study competition among methods for analyzing large spatial data. *J Agric Biol Environ Stat* 24: 398-425
- Katzfuss M, Guinness J (2021) A general framework for Vecchia approximations of Gaussian processes. *Stat Sci* 36: 124–141
- Kumar S, Mohri M, Talwalkar A (2012) Sampling methods for the Nyström method. *J Mach Learn Res* 13: 981-1006
- LeSage JP, Pace RK (2009) *Introduction to Spatial Econometrics*. Chapman and Hall/CRC
- Liu H, Ong YS, Shen X, Cai J (2020) When Gaussian process meets big data: A review of scalable GPs. *IEEE Trans Neural Netw Learn Syst* 31: 4405–4423

- Lu B, Yang W, Ge Y, Harris P (2018) Improvements to the calibration of a geographically weighted regression with parameter-specific distance metrics and bandwidths. *Comput Environ Urban Syst* 71: 41-57
- Meinshausen N, Ridgeway G (2006) Quantile regression forests. *J Mach Learn Res* 7: 983-999
- Murakami D, Griffith DA (2015) Random effects specifications in eigenvector spatial filtering: A simulation study. *J Geogr Syst* 17: 311–331
- Murakami D, Sugawara S, Seya H, Griffith DA (2024) Sub-model aggregation for scalable eigenvector spatial filtering: Application to spatially varying coefficient modeling. *Geogr Anal*: 56: 768-798
- Murakami D, Shirota S, Kajita S, Kajita M (2025) Fast spatio-temporally varying coefficient modeling with reluctant interaction selection. *Geogr Anal* 57: 521–539
- Sigrist F (2022) Gaussian process boosting. *J Mach Learn Res* 23: 1-46
- Soviany P, Ionescu RT, Rota P, Sebe N (2022) Curriculum learning: A survey. *Int J Comp Vis* 130: 1526–1565
- Williams C, Rasmussen C (1995) Gaussian processes for regression. *Adv Neural Inf Process Syst* 8: 514-520
- Wood SN (2017) *Generalized Additive Models: An Introduction with R* (2nd ed.). Chapman & Hall/CRC, New York

- Wood SN, Li Z, Shaddick G, Augustin NH (2017) Generalized additive models for gigadata: Modeling the UK black smoke network daily data. *J Am Stat Assoc* 112: 1199–1210
- Yoshida T, Murakami D, Seya H (2024) Spatial prediction of apartment rent using regression-based and machine learning-based approaches with a large dataset. *J Real Estate Finance Econ* 69: 1–28
- Zammit-Mangion A, Ng TLJ, Vu Q, Filippone M (2022) Deep compositional spatial models. *J Am Stat Assoc* 117: 1787–1808
- Zhan W, Datta A (2025) Neural networks for geospatial data. *J Am Stat Assoc* 120: 535–547